Modeling and inverse compensation of dynamics of base-excited ionic polymer–metal composite sensors

Hong Lei, Chaiyong Lim and Xiaobo Tan

Abstract
Motivated by their structural monitoring and energy harvesting applications, in this article, we study the modeling and inverse compensation of cantilevered ionic polymer–metal composite sensors that are excited at base. The proposed dynamic model is physics based, combines the vibration dynamics of a flexible beam under base excitation and the ion transport dynamics within an ionic polymer–metal composite, and incorporates the effect of a tip mass. Excellent agreement is demonstrated between the model prediction and experimental measurement in both the magnitude and the phase of the frequency response, for the frequency range of 10–150 Hz. For the purpose of real-time signal processing, we further reduce the model to finite dimension by combining techniques of Padé approximation and Taylor series expansion. For the reconstruction of the base excitation signal given the sensor output, we present an inverse compensation scheme for the reduced sensor model, where stable but noncausal inversion and leaky integration are introduced to deal with zeros that are unstable and on the imaginary axis, respectively. The effectiveness of the scheme as well as the underlying model is validated experimentally in the reconstruction of structural vibration signals, when the structure to which the ionic polymer–metal composite is attached is subjected both to periodic vibrations and to an impact.

Keywords
Ionic polymer–metal composite, ionic polymer–metal composite sensor, dynamic model, base-excited flexible beam, structural vibration monitoring, electroactive polymer

Introduction

Electroactive polymers (EAPs) have received tremendous interest for their potential applications in a large variety of engineering areas (Bar-Cohen, 2001). Ionic polymer–metal composites (IPMCs) are an important class of EAPs with built-in actuation and sensing capabilities. They hold strong promise for versatile applications because they require low-actuation voltages (several volts) for producing large bending deformation, work in air and in aqueous environments without stringent packaging requirements, and have minimal structural complexity in implementation as actuators and sensors (Shahinpoor and Kim, 2001, 2004). They are also biocompatible and amenable to microfabrication (Chen and Tan, 2010; Lei et al., 2012a).

An IPMC sample typically consists of a thin ion-exchange membrane (e.g. Nafion), chemically plated with a noble metal as electrodes on both surfaces. The traditional method for the fabrication of IPMCs is based on the impregnation–reduction–ion-exchange process (Kim and Shahinpoor, 2003). Inside the polymer, anions covalently fixed to polymer chains are balanced by mobile

cations. An applied voltage across the IPMC leads to the redistribution of cations and accompanying solvent molecules, resulting in both differential swelling and electrostatic forces, which cause the material to bend and hence the actuation effect (Nemat-Nasser and Li, 2000; Shahinpoor and Kim, 2001; Wallmersperger et al., 2007). IPMC actuators have been proposed for various applications in biomedical devices (Chen et al., 2007a), grippers and manipulation systems (Tadokoro et al., 1999), and biomimetic robotics (Aureli et al., 2010a; Chen et al., 2010). However, IPMCs have inherent sensing properties—an applied force or deformation on an IPMC beam yields a detectable electrical signal (typically open-circuit voltage or short-circuit current) across the

Smart Microsystems Laboratory, Department of Electrical and Computer Engineering, Michigan State University, East Lansing, MI, USA

Corresponding author:
Xiaobo Tan, Smart Microsystems Laboratory, Department of Electrical and Computer Engineering, Michigan State University, 428 S. Shaw Lane, Engineering Building B320, East Lansing, MI 48824, USA.
Email: xbtan@egr.msu.edu

electrodes. Recent applications of IPMC sensing capability span measurement of force, pressure, displacement and shear loading; structural health monitoring; and energy harvesting (Abdulsadda and Tan, 2011, 2012; Abdulsadda et al., 2011; Aureli et al., 2010; Bahramzadeh and Shahinpoor, 2011; Bonomo et al., 2008; Brufau-Penella et al., 2008; Farinholt et al., 2009; Lim et al., 2012; Paola et al., 2008; Peterson and Porfiri, 2012; Zangrilli and Weiland, 2011).

There has been extensive effort in modeling and understanding IPMC sensors in recent years. Newbury and Leo proposed a gray-box model for the IPMC actuators and sensors by drawing analogy to piezoelectric transducers (Newbury, 2002; Newbury and Leo, 2002). The latter model was further elaborated and verified by Bonomo et al. (2006), and Takagi et al. (2008) examined the modeling of IPMC sensors using the current and voltage as the output based on Onsager's equation. Buechler and Leo (2007) presented a variational formulation to model IPMCs and evaluated the model computationally with the Galerkin method. Various physics-based models have also been studied for IPMCs. For example, De Gennes et al. (2000) used linear irreversible thermodynamics to study IPMC transduction, where a static model was proposed to capture both actuation and sensing mechanisms. Through a micromechanics approach, Nemat-Nasser and Li (2000) presented a partial differential equation (PDE) governing the charge dynamics in IPMC materials. This model was used by Farinholt and Leo (2004) to derive the charge sensing response for a cantilevered IPMC beam subject to tip displacement. With the same governing PDE from Nemat-Nasser and Li (2000), Chen et al. (2007b) developed a geometrically scalable, infinite-dimensional transfer function model for cantilevered IPMC sensors subjected to tip stimulus, where the effect of distributed surface resistance of IPMC electrodes is captured. Porfiri (2009) developed a comprehensive framework for modeling IPMC actuation and sensing based on mixture theory (Bufalo et al., 2008), which was specialized to the analysis of linear static deformation of a thin and flat IPMC. Aureli and Porfiri (2013) further extended the modeling framework for IPMC sensing to account for convection and large deformations.

Various configurations of IPMC sensors have been considered in the literature. The most common configuration is an IPMC cantilever beam, where the stimulus is applied at the free end of the beam. Integrating multiple IPMC sensors in an array results in an artificial lateral line system for flow sensing, as reported by Abdulsadda and Tan (2011, 2012) and Abdulsadda et al. (2011). An IPMC undergoing longitudinal vibrations has been proposed for energy harvesting (Farinholt et al., 2009). A dynamic curvature sensor has been created by bonding an IPMC to the surface of a structure (Bahramzadeh and Shahinpoor, 2011).

Another important configuration for IPMC sensors is a cantilevered IPMC subjected to base excitation, which finds potential applications in energy harvesting and structural monitoring (Aureli et al., 2010b; Brufau-Penella et al., 2008; Paola et al., 2008). Paola et al. (2008) examined vibration sensing of an IPMC beam with a tip mass, where the IPMC was subjected to excitation at the fixed end (base). They modeled the mechanoelectric response of an IPMC with a linear black-box model, where the input is the relative displacement of the tip, calculated by subtracting the absolute base displacement from the absolute tip displacement. In Brufau-Penella et al.'s (2008) study, an IPMC strip under base excitation in air is studied for energy harvesting. The vibration dynamics of the strip is modeled as an Euler–Bernoulli beam. The mechanical strain of the fundamental vibration mode is converted into a short-circuit current or an open-circuit voltage through a gray-box model of the IPMC. The transfer function relating the short-circuit current to the base excitation is derived, but not in a closed form. Experimental results are compared with the model prediction, indicating good agreement for the magnitude response between 5 Hz and the first resonant frequency, which is around 25 Hz, but no comparison is given on the phase response. In Aureli et al. (2010b), energy harvesting of an IPMC immersed in a fluid environment and subjected to underwater base excitation is studied. Euler–Bernoulli beam theory is used to model the mechanical multimodal vibration of the IPMC strip. A linearized solution of the Navier–Stokes equation is used to describe the effect of the encompassing fluid on the IPMC vibration. A physics-based model is presented to describe the dynamic chemo-electric response of the IPMC, based on the Poisson–Nernst–Planck model. The overall sensing model has a good agreement with the measured magnitude response from 2 to 50 Hz. The same data on IPMC base excitation in Aureli et al. (2010b) are further analyzed based on an approach that extends Sader's (1998) theory of beam vibration in viscous fluids for small amplitudes of oscillations to large amplitudes by incorporating the effect of vibration amplitude and frequency on the hydrodynamic function (Aureli et al., 2012; Aureli and Porfiri, 2010).

The main contributions of this article are twofold. The first contribution is a dynamic, physics-based model for a base-excited IPMC sensor loaded with a tip mass, which has a closed-form expression. The model combines the vibration dynamics of a flexible beam with a tip mass under base excitation and the ion transport dynamics within the IPMC. The mechanical vibration of the IPMC is modeled with Euler–Bernoulli cantilever beam theory, incorporating damping and accommodating suitable boundary conditions (BCs). The ion transport dynamics is based on the governing PDE in Nemat-Nasser and Li (2000) that accounts for electrostatic interactions, ionic diffusion, and ionic

migration along the thickness direction. To relate the mechanical deformation to charge dynamics within the IPMC, an assumption analogous to that by Farinholt and Leo (2004) is made as follows: at the boundary, the charge distribution is proportional to the externally applied stress. The derived model for IPMC sensor relates the short-circuit sensing current to the mechanical base excitation and takes the form of an infinite-dimensional transfer function involving hyperbolic and square-root terms. Expressed in terms of fundamental physical parameters and sensor dimensions, this transfer function model is geometrically scalable. Experimental results indicate that the proposed model captures well both the magnitude and phase responses of the sensor from 10 to 150 Hz. While the aforementioned frequency range is primarily determined by limitations of the experimental setup, it already covers the range of interest for many applications. In addition, the model predicts that a tip mass can be used to effectively tune the resonant frequencies of the vibration and sensing dynamics, which is confirmed by experimental results.

The second contribution of this work is an inverse compensation scheme for the proposed model, for the reconstruction of base excitation signals given the sensor output. For the purpose of real-time signal processing, we reduce the original infinite-dimensional model to finite-dimension by combining techniques of Padé approximation and Taylor series expansion. The model is of nonminimum phase (having zeros in the right half plane) and is nonhyperbolic (with a zero at the origin) and thus presents challenges in the inversion. These challenges are addressed with stable but noncausal inversion and leaky integration. The effectiveness of the proposed compensation scheme as well as the underlying model is validated experimentally in the reconstruction of structural vibration signals, when the structure to which the IPMC is attached is subjected both to periodic vibrations and to an impact.

The remainder of this article is organized as follows. In section "Model derivation," the dynamic model for the base-excited IPMC sensor with a tip mass is derived. Experimental results on model validation are presented in section "Experimental model validation." Model reduction is discussed in section "Model reduction." The inversion algorithm is presented and validated with simulation and structural vibration monitoring experiments in section "Inverse compensation scheme." Finally, concluding remarks are provided in section "Conclusion."

Model derivation

Mechanical dynamics of a base-excited cantilever beam

Consider Figure 1, where the beam is clamped at one end ($z = 0$) and is subjected to a base excitation $u(t)$,
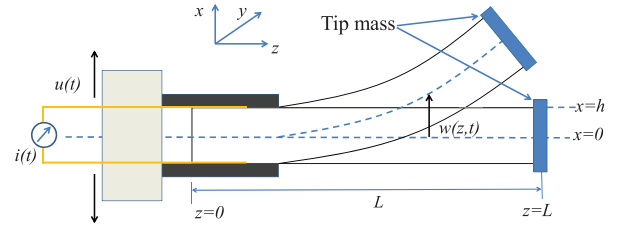

Figure 1. Geometric definition of an IPMC beam subjected to base excitation.
IPMC: ionic polymer–metal composite.

producing the bending displacement $w(z,t)$ and a short-circuit sensing current $i(t)$. The neutral axis of the beam is denoted by $x = 0$, and the upper and lower surfaces are denoted by $x = h$ and $x = -h$, respectively. The $y - z$ plane is parallel to the beam plane when the beam is not deformed. We consider that a mass of M_L is located at the beam tip $z = L$. We assume that the beam mass and the tip mass are considerably small and their gravity effects are ignored, which implies the skew symmetry of the axial stress. We further assume that the IPMC undergoes small deformation when vibrating, the deformation is restricted to the $x - z$ plane, and the IPMC beam has a considerably smaller thickness $2h$ than its length L and width b. Therefore, the displacement $w(z,t)$ of the beam can be described by the following Euler–Bernoulli beam equation with viscous air damping and strain-rate (or Kelvin–Voigt) damping (Clough and Penzien, 1975; Erturk and Inman, 2011)

$$YI\frac{\partial^4 w(z,t)}{\partial z^4} + C_s I\frac{\partial^5 w(z,t)}{\partial z^4 \partial t} + C_a \frac{\partial w(z,t)}{\partial t} + m\frac{\partial^2 w(z,t)}{\partial t^2} = 0 \tag{1}$$

where Y is Young's modulus, $I = 2/3(bh^3)$ is the moment of inertia of the beam cross section, C_a is the viscous air damping coefficient, C_s is the strain-rate damping coefficient, and m is the mass per unit length of the beam. It is a simple approach to use viscous air damping to model the force of air particles that acts on the beam during the vibration. The composite structure of the IPMC is assumed to demonstrate linear-viscoelastic material behavior; hence, the strain-rate damping is included in equation (1), accounting for the structural damping due to the internal energy dissipation of the beam. These two mechanisms of damping meet the proportional damping criterion, and for the later model analysis, they are also mathematically convenient (Erturk and Inman, 2011).

Performing the Laplace transform on the time variable t, we convert equation (1) into the Laplace domain

$$(YI + C_s Is)\frac{\partial^4 W(z,s)}{\partial z^4} + (C_a s + ms^2)W(z,s) = 0 \tag{2}$$

where s is the Laplace variable. Equation (2) can be rewritten as

$$\frac{\partial^4 W(z,s)}{\partial z^4} + 4k(s)^4 s^2 W(z,s) = 0 \qquad (3)$$

where $k(s)^4 = C_a + ms/4Is(Y + C_s s)$. The general solution for equation (3) is given as follows

$$\begin{aligned} W(z,s) = &\ A_1(z,s)\cos(pz)\cosh(pz) \\ &+ A_2(z,s)\cos(pz)\sinh(pz) \\ &+ A_3(z,s)\sin(pz)\cosh(pz) \\ &+ A_4(z,s)\sin(pz)\sinh(pz) \end{aligned} \qquad (4)$$

where $p = k\sqrt{s}$. We consider the following BCs

$$w(0,t) = u(t) \qquad (5)$$

$$\frac{\partial w(0,t)}{\partial z} = 0 \qquad (6)$$

$$I_L \frac{\partial^3 w(L,t)}{\partial t^2 \partial z} + \frac{\partial^2 w(L,t)}{\partial z^2} = 0 \qquad (7)$$

$$YI \frac{\partial^3 w(L,t)}{\partial z^3} - M_L \frac{\partial^3 w(L,t)}{\partial t^3} = 0 \qquad (8)$$

or equivalently

$$W(0,s) = U(s) \qquad (9)$$

$$\frac{\partial W(0,s)}{\partial z} = 0 \qquad (10)$$

$$s^2 I_L \frac{\partial W(L,s)}{\partial z} + \frac{\partial^2 W(L,s)}{\partial z^2} = 0 \qquad (11)$$

$$\frac{\partial^3 W(L,s)}{\partial z^3} - \gamma(s) W(L,s) = 0 \qquad (12)$$

where $\gamma(s) = s^3 M_L / YI$ and I_L is the moment of inertia of the tip mass about $z = L$. For the geometric BCs at $z = 0$ (clamped base), the first BC (5) means that the base displacement is prescribed by the excitation $u(t)$ ($U(s)$), and the second BC (6) indicates the fixed slope of zero. For the natural BCs at $z = L$ (free end), the third BC (7) indicates the zero bending moment, and equation (8) means that the internal shear force is in equilibrium with the force applied by the mass at the tip (Erturk and Inman, 2011). The moment of inertia of the tip mass attachment I_L is ignored in equation (7) based on the assumption that the attachment is a point mass right on the tip.

By substituting the BCs into equation (4), we get the following equation for the transformed displacement

$$W(z,s) = U(s) \frac{N_1(z,s)}{D_1(s)} \qquad (13)$$

where

$$\begin{aligned} N_1(z,s) = &\ D_1(s)[\cos(pz)\cosh(pz) - \sin(pz)\sinh(pz)G_1(s)] \\ &+ [C_1(s) + C_2(s)G_1(s)][\cosh(pz)\sin(pz) \\ &- \cos(pz)\sinh(pz)] \end{aligned} \qquad (14)$$

$$C_1(s) = \sin(pL)\sinh(pL) \qquad (15)$$

$$C_2(s) = \cos(pL)\cosh(pL) \qquad (16)$$

$$G_1(s) = \frac{\gamma(s)(\sin(2pL) + \sinh(2pL)) + 2p^3(\cosh(2pL) - \cos(2pL))}{\gamma(s)(\sinh(2pL) - \sin(2pL)) + 2p^3(\cos(2pL) + \cosh(2pL) + 2)} \qquad (17)$$

$$D_1(s) = \cos(pL)\sinh(pL) + \cosh(pL)\sin(pL) \qquad (18)$$

Following Clough and Penzien (1975), we can decompose $W(z,s)$ as

$$W(z,s) = W^s(z,s) + W^d(z,s) \qquad (19)$$

where $W^s(z,s)$ is the quasi-static displacement due to the base motion, $W^s(z,s) = U(s)$, and $W^d(z,s)$ is the dynamic displacement due to dynamic inertial and viscous force effects. The axial strain in the IPMC beam is only produced by $W^d(z,s)$

$$W^d(z,s) = U(s) \frac{N_1(z,s)}{D_1(s)} - U(s) \qquad (20)$$

Charge dynamics in the IPMC

The governing PDE for charge distribution within IPMC was first proposed by Nemat-Nasser and Li (2000). Since the thickness of the IPMC beam is much smaller than its length or width, it can be assumed that the electric field E inside the polymer is restricted to the thickness direction (x-direction) (Chen et al., 2007b). Following the derivation by Chen et al. (2007b), we obtain the linearized PDE for the charge density distribution $\rho(x,z,t)$

$$\frac{\rho(x,z,t)}{\partial t} - d \frac{\partial^2 \rho(x,z,t)}{\partial x^2} + \frac{F^2 dC^-}{\kappa_e RT}(1 - C^- \Delta V)\rho(x,z,t) = 0 \qquad (21)$$

where d is the ionic diffusivity, F is Faraday's constant, C^- is the anion concentration (mol m^{-3}), κ_e is the effective dielectric constant of the polymer, R is the gas constant, T is the absolute temperature, and ΔV is the volumetric change, which represents how much the polymer volume swells after taking water. Since the anions are permanently attached to the backbone structure, C^- is assumed to be spatially homogeneous. Furthermore, in the absence of large changes in the hydration level (as in the context considered in our work), it is reasonable to assume that C^- is a constant.

Equation (21) can be converted into the Laplace domain

$$\frac{\partial^2 \rho(x,z,s)}{\partial x^2} - \beta(s)^2 \rho(x,z,s) = 0 \qquad (22)$$

where $\beta(s)^2 = (s + K)/d$ and $K \triangleq (F^2 dC^-/\kappa_e RT)(1 - C^- \Delta V)$. The general solution of equation (22) takes the form

$$\rho(x,z,s) = a_1(z,s)\,e^{-\beta(s)x} + a_2(z,s)\,e^{\beta(s)x} \qquad (23)$$

where $a_1(z,s)$ and $a_2(z,s)$ depend on the BCs.

The sensing model

Following Farinholt and Leo (2004) and Chen et al. (2007b), we assume that the charge density $\rho(x,z,s)$ is proportional to the mechanically induced stress $\sigma(x,z,s)$ at the boundary $x = \pm h$

$$\sigma(\pm h,z,s) = \alpha_o \rho(\pm h,z,s) \qquad (24)$$

where α_o is the charge–stress coupling constant. From the fact that $\sigma(h,z,s) + \sigma(-h,z,s) = 0$, one gets $\rho(h,z,s) + \rho(-h,z,s) = 0$, which implies that $a_1(z,s) = -a_2(z,s)$. Consequently, equation (23) becomes

$$\rho(x,z,s) = 2a_2(z,s)\sinh(\beta(s)x) \qquad (25)$$

We can further relate the stress σ to the external stimulus $U(s)$

$$\sigma(x,z,s) = \frac{M(z,s)x}{I} \qquad (26)$$

where $M(z,s)$ denotes the bending moment at z, which can be written as

$$M(z,s) = YI\frac{\partial^2 W^d(z,s)}{\partial z^2}$$
$$= YI\frac{U(s)}{D_1(s)}\frac{\partial^2 N_1(z,s)}{\partial z^2} \qquad (27)$$

Define

$$N_2(z,s) \triangleq \frac{\partial^2 N_1(z,s)}{\partial z^2} \qquad (28)$$

We can then write

$$\sigma(x,z,s) = \frac{YxU(s)N_2(z,s)}{D_1(s)} \qquad (29)$$

Using equations (25) and (29) at $x = h$, we can solve for $a_2(z,s)$

$$a_2(z,s) = \frac{YhU(s)N_2(z,s)}{2\alpha_o D_1(s)\sinh(\beta(s)h)} \qquad (30)$$

Finally, let E and ϕ denote the electric field and electric potential, respectively. The following equations hold

$$E(x,z,s) = -\frac{\partial \phi(x,z,s)}{\partial x}$$
$$\kappa_e \frac{\partial E(x,z,s)}{\partial x} = \rho(x,z,s)$$

With these equations and equation (25), we can solve for $E(x,z,s)$ using the short-circuit BC $\phi(h,z,s) - \phi(-h,z,s) = 0$. Note that here we assume perfectly conducting electrodes for the IPMC. In later experiments, the latter assumption is satisfied by further depositing gold on the electrodes to greatly reduce the surface resistance. The resulting electric field is evaluated as

$$E(x,z,s) = \frac{2a_2(z,s)\cosh(\beta(s)x)}{\kappa_e\beta(s)} - 2a_2(z,s)\frac{\sinh(\beta(s)h)}{\kappa_e h\beta^2(s)} \qquad (31)$$

The total induced charge can be obtained by integrating the electric displacement $D = \kappa_e E$ over the beam area at the boundary $x = h$

$$Q(s) = \frac{bY(\beta(s)h\coth(\beta(s)h) - 1)U(s)}{\alpha_o D_1(s)\beta^2(s)}N_3(s) \qquad (32)$$

where

$$N_3(s) = \int_0^L N_2(z,s)dz$$
$$= 2p(s)[C_1(s) + C_2(s)G_1(s)]\sin(p(s)L)\sinh(p(s)L)$$
$$- D_1(s)p(s)[\cosh(p(s)L)\sin(p(s)L)(G_1(s) + 1)$$
$$+ \cos(p(s)L)\sinh(p(s)L)(G_1(s) - 1)]$$

Finally, the transfer function for the sensor, taking the base stimulus $U(s)$ as input and the short-circuit current $I(s)$ as output, is
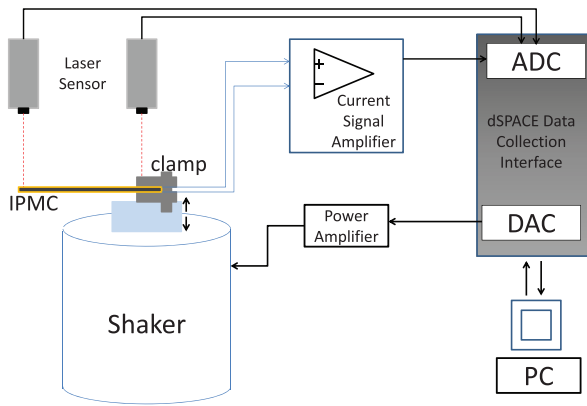
$$H(s) = \frac{I(s)}{U(s)} = \frac{sQ(s)}{U(s)}$$
$$= \frac{bYs(\beta(s)h\coth(\beta(s)h) - 1)}{\alpha_o\beta^2(s)}\frac{N_3(s)}{D_1(s)} \qquad (33)$$

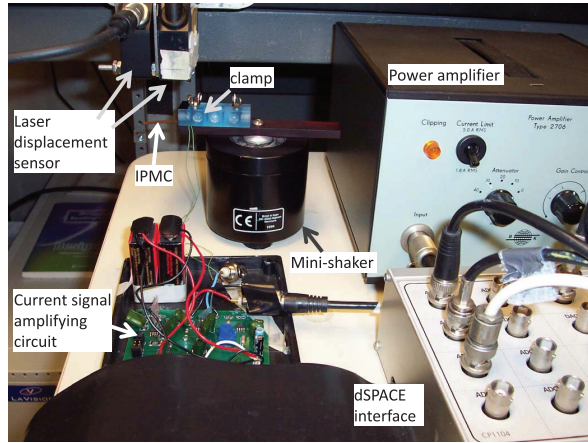For the special case of zero tip mass, $M_L = 0$, $\gamma(s) = 0$, $G_1(s)$ becomes

$$G_1(s) = \frac{\cosh(2p(s)L) - \cos(2p(s)L)}{\cos(2p(s)L) + \cosh(2p(s)L) + 2}$$

and $H(s)$ is evaluated as

$$H(s) = \frac{bYs(\beta(s)h\coth(\beta(s)h) - 1)}{\alpha_o\beta^2(s)}\frac{N'_3(s)}{D'_1(s)} \qquad (34)$$

Figure 2. The (a) schematic and (b) photograph of the experimental setup for model validation.
IPMC: ionic polymer–metal composite; ADC: analog-to-digital converter; DAC: digital-to-analog converter; PC: personal computer.

Table 1. Physical constants and directly measured parameters

F (C mol^{-1})	R (J mol^{-1} K^{-1})	T (K)	L (mm)	b (mm)	h (μm)	m (kg m^{-1})
96,487	8.3143	300	29.45	6.05	160	3.797×10^{-3}

where

$$N'_3(s) = 2p(s)[\cos(p(s)L)\sinh(p(s)L) \\ - \cosh(p(s)L)\sin(p(s)L)] \quad (35)$$

$$D'_1(s) = \cos(p(s)L)^2 + \cosh(p(s)L)^2 \quad (36)$$

Experimental model validation

Experimental setup

Figure 2(a) and (b) shows the schematic and the photograph of the experimental setup, which can provide base excitation for a cantilevered IPMC beam and allow the measurement of base displacement, tip displacement, and the IPMC sensing current. An IPMC beam with a tip mass is clamped at the base by two rigid bars, and the bars are fixed on a mini-shaker (Type 4810; Brüel & Kjær), which generates vibration stimulus (up and down) with some controlled frequency. A narrow strip of the tape, used as the tip mass, is wrapped around the free end of the IPMC beam. The weight of the tip mass is controlled by the length of the tape strip. In order to verify the beam dynamics and identify some mechanical parameters, two laser displacement sensors (OADM 20I6441/S14F; Baumer Electric) are mounted above the IPMC beam, one measuring the tip displacement, while the other measuring the base displacement. The mounting frame for the laser sensors is isolated from the table where the mini-shaker is mounted. A

two-tier amplification circuit is used to measure the short-circuit current generated by the IPMC. Control signal generation, sensing data acquisition, and processing are performed through a dSPACE system (RTI 1104; dSPACE). The IPMC sample used in this article was obtained from Environmental Robots Inc. and then deposited with a layer of gold (0.2 mm thick) on each side in the electron beam physical vapor deposition system (Kurt Lesker AXXIS™ PVD system), which significantly reduced the surface resistance. The dimensions of the sample are given in Table 1. Its surface resistance was reduced from 65 to about 2 Ω after gold deposition, which justifies the assumption of perfectly conducting electrodes used in the modeling part.

Parameter identification and model validation

Table 1 lists the physical constants and the parameters obtained through direct measurement. The temperature is read directly from the thermometer in the room. The geometric dimensions, including length, width, and thickness, are measured with a vernier caliper. For both width and thickness, multiple measurements are conducted at different points along the IPMC sample, and the average values are adopted. The mass per unit length of the beam is calculated by dividing the weight of the sample, which is obtained with a precision electronic balance, by the sample length. The parameters that remain to be determined include Young's modulus Y, viscous air damping coefficient C_a, strain-rate
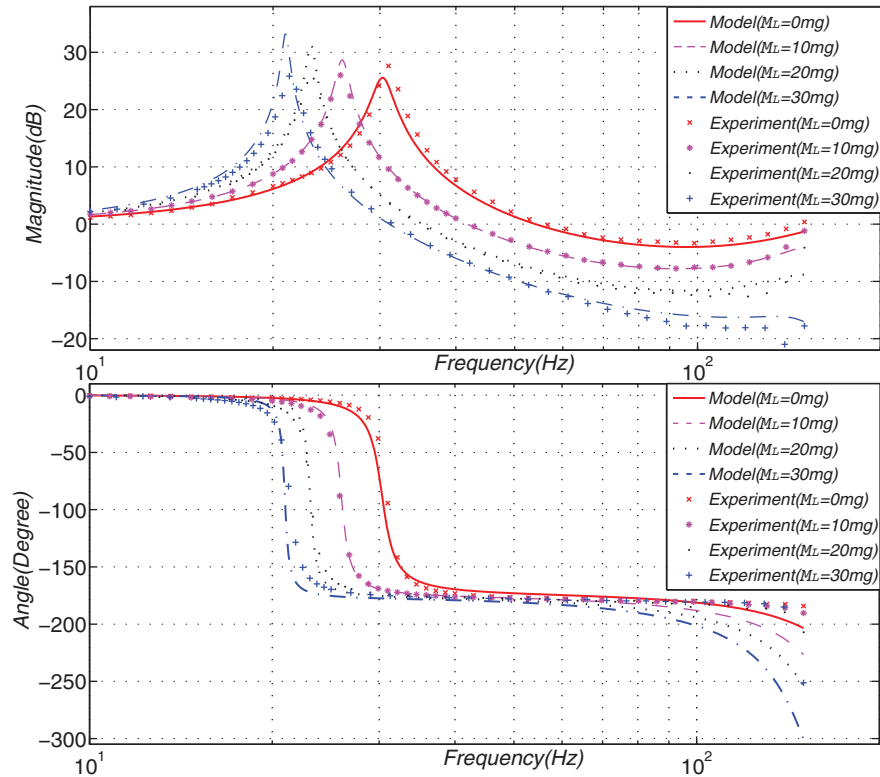
Figure 3. Comparison of the measured frequency responses with model predictions for different tip masses (0, 10, 20, and 30 mg): mechanical dynamics (input: base excitation; output: tip displacement).

damping coefficient C_s, diffusion coefficient d, anion concentration C^-, dielectric constant κ_e, and charge–stress coupling constant α_o.

Considering that there are as many as seven parameters to be identified, it is better to separate Young's modulus Y, viscous air damping coefficient C_a, and strain-rate damping coefficient C_s from other parameters, and identify these three first, since they can be determined using only the base-excited beam dynamics as shown in equation (13). To be specific, we fix an excitation frequency f and acquire the base vibration $u(t)$ and tip mechanical deformation $w(L,t)$. Both $u(t)$ and $w(L,t)$ are measured by the laser sensors. The amplitudes and phases of these two signals are extracted through fast Fourier transform and then used to compute the magnitude gain and phase shift of the beam dynamics at that particular frequency. Repeating this process for other actuation frequencies results in the empirical frequency response for the beam dynamics. Our experimental setup allows reliable control and signal acquisition for the excitation frequency range of 10–150 Hz. The lower frequency bound is determined by the mini-shaker characteristics, while the upper bound is determined by the response time of the laser sensors (close to 1 ms). Despite the limitation, this frequency range covers the relevant frequency spectrum of many applications that are of interest. The three parameters

Y, C_s, and C_a are tuned by curve-fitting the frequency response of the mechanical dynamics using the MATLAB function *fminsearch*. Once Y and C_s are identified, they are plugged into $H(s)$ for estimating the four remaining parameters using a similar curve-fitting strategy for the sensing model.

Figure 3 shows the result of curve-fitting for the mechanical model, $W(L,s)/U(s)$, and Figure 4 shows the result of curve-fitting for the sensing model, $H(s)$. For each figure, there are four groups of experimental results, one of which corresponds to the IPMC sample without tip mass, while the other three correspond to the same sample with different tip masses (10, 20, and 30 mg). Only the experimental data without tip mass were used for parameter identification. Then, the identified parameters are applied to predict the frequency response of the mechanical and sensing dynamics of the IPMC sensor with different tip masses. All the identified parameters are listed in Table 2. Generally, they have good agreement with the values reported in the literature (Chen et al., 2007b; Farinholt and Leo, 2004; Nemat-Nasser and Li, 2000), while the moderate parameter discrepancies can be explained by the fact that the IPMC sample used in this article is different and is tested in different ambient environments (humidity, temperature) from those reported in the literature. The identified in-air damping coefficient C_a is very small
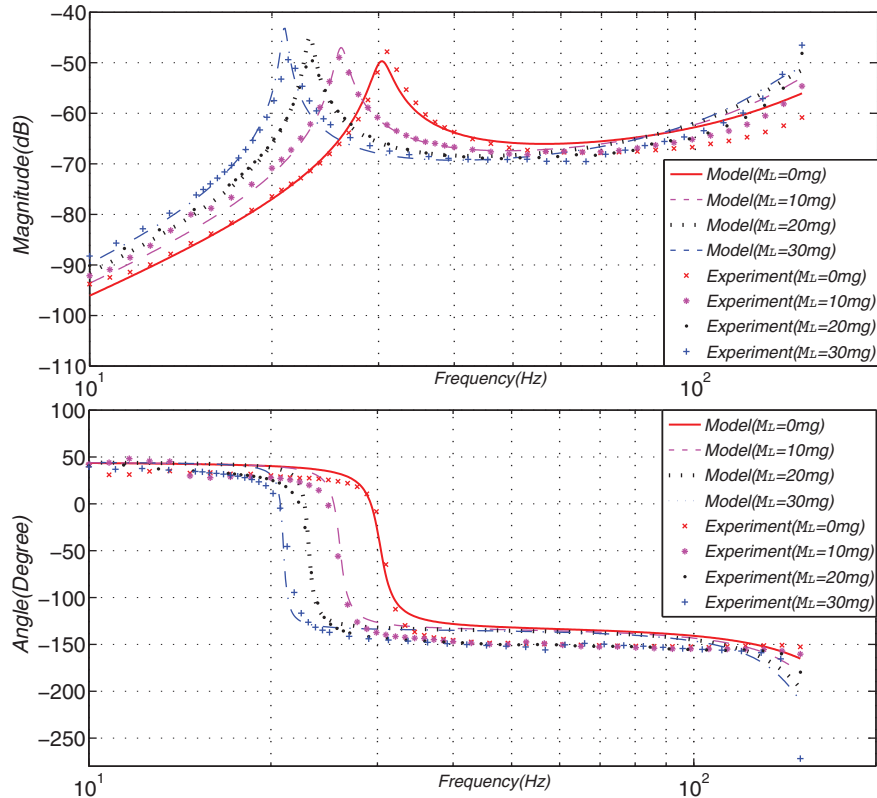
Figure 4. Comparison of the measured frequency responses with model predictions for different tip masses (0, 10, 20, and 30 mg): sensing dynamics (input: base excitation; output: IPMC short-circuit current).
IPMC: ionic polymer–metal composite.

Table 2. Identified parameters by curve-fitting

Y (Pa)	C_a (kg m^{-1} s^{-1})	C_s (Pa s)	d (m^2 s^{-1})	C^- (mol m^{-3})	κ_e (F m^{-1})	α_o (J C^{-1})
5.116×10^8	0.024	1.91×10^5	1.973×10^{-15}	1085	1.07×10^{-3}	94.64

and can be neglected without affecting the model prediction too much, which is assumed to be so in some literature (Brufau-Penella et al., 2008).

As shown in Figures 3 and 4, although the parameters are fitted based on one group of experimental data in the case of zero tip mass, the model predictions match well the experimental data for all the four cases with different tip masses, over the considered frequency range, for both the magnitude and phase responses, which provides strong support for the physical nature of the proposed modeling approach. The discrepancies between the model prediction and the experimental data are attributed to idealistic assumptions in the modeling that are not fully satisfied by the experimental setup, uncertainties in ambient environmental conditions including the temperature and the humidity, and bandwidth limitations of the laser sensors. Both the temperature (Ganley et al., 2011) and the humidity (Brunetto et al., 2011) influence the dynamic behavior of an IPMC. There are several approaches that can be adopted to mitigate the impact of environmental

variations and improve the model accuracy. For example, one can follow a similar approach proposed by Ganley et al. (2011) to characterize the temperature/humidity dependence of the physical parameters, to approximate such dependencies with simple functions such as polynomials, and then to use auxiliary measurements of temperature and/or humidity to obtain the corresponding parameters. The influence of humidity can also be greatly reduced by encapsulating the IPMC with materials such as parylene to set up barriers against water permeation (Lei et al., 2012b).

Given Young's modulus and the beam dimensions, the natural frequencies for a base-excited cantilever beam with zero tip mass can be calculated by the following formula

$$f = \frac{R_{ch}^2}{2\pi} \sqrt{\frac{YI}{mL^4}} \qquad (37)$$

where R_{ch} is the root of the characteristic equation, with the value of 1.8751 and 4.6941 for the first mode and

second mode, respectively (Ghosh, 1986). By plugging the sample dimensions given in Table 1 and Young's modulus in Table 2 into (37), we get the natural frequency of 30 Hz for the first-mode vibration of the proposed IPMC sample with zero tip mass and 189 Hz for the second mode. Limited by the response time of the laser displacement sensors, which determines the upper bound of the excitation frequency for reliable motion measurement, the considered frequency range is up to 150 Hz, in which the second mode has also been activated, as can be observed from the magnitude and phase responses beyond 100 Hz in Figure 3. We suspect that the relatively large phase discrepancies between the model and the experimental measurement in the higher frequency range close to 150 Hz are due to the less precise laser measurement.

From Figures 3 and 4, we can clearly see how the tip mass influences the mechanical and sensing dynamics of the IPMC sensor by changing its gain and resonant frequency. In particular, with larger tip mass, the resonant frequency is lower. This observation will be useful for real applications, where one can tune the tip mass to make the resonant frequency close to the dominant frequencies in the excitation stimuli, to maximize the sensor response.

Model reduction

The sensing model $H(s)$, shown in equation (33), is infinite-dimensional since it involves nonrational functions such as $\sinh(\cdot)$, $\cosh(\cdot)$, and $\sqrt{\cdot}$. For practical use of the model, it is of interest to reduce the model to a finite order. Without losing generality, we will focus on the case of zero tip mass for ease of presentation. We first decompose $H(s)$ as $H(s) = H^E(s) \cdot H^M(s)$, where

$$H^E(s) = \frac{sbY[\beta(s)h\coth(\beta(s)h) - 1]}{\alpha_o\beta^2(s)}, \quad H^M(s) = \frac{N'_3(s)}{D'_1(s)} \tag{38}$$

Note that H^M and H^E are related to the mechanical and electrical dynamics, respectively. First, consider H^E. Since $|C^-\Delta V| \ll 1$ (Nemat-Nasser and Li, 2000), we take $1 - C^-\Delta V \approx 1$. Based on the physical parameters (see Tables 1 and 2 in section "Experimental model validation"), for $s = j\omega$, one has $|\beta(s)| = |\sqrt{(s + K)/d}| > 10^6$, when the angular frequency ω is relatively low. Furthermore, we have $\coth(\beta(s)h) \approx 1$. $H^E(s)$ can then be simplified as

$$H^E(s) \approx \frac{sbY(\beta(s)h - 1)}{\alpha_o\beta^2(s)} = \frac{sbY\sqrt{d}(\sqrt{s + K}h - \sqrt{d})}{\alpha_o(s + K)} \tag{39}$$

We need to further approximate $\sqrt{s + K}$ with a rational function of s. After comparing with the approximation result using Taylor series expansion, we

have found that Padé approximation (Baker and Graves-Morris, 1996) provides better performance. Given a function of $f(s)$ and two integers $m \geq 0$ and $n \geq 1$, the Padé approximation of order (m/n) around a point s_0 is the rational function $P_{m,n}(s - s_0)$

$$f(s) \approx P_{m,n}(s - s_0) = \frac{\sum_{l=0}^{m} q_l(s - s_0)^l}{1 + \sum_{k=1}^{n} d_k(s - s_0)^k} \tag{40}$$

It is found that the Padé approximation of the order $(3/2)$ can provide adequate approximation with minimal complexity for $\sqrt{s + K}$ around some point s_0, where $s_0 = |j\omega_0|$ and ω_0 is close to the midpoint of the angular frequency range one is interested in. In this article, we take $s_0 = 500$ because the frequency range considered in our experiments is from 10 to 150 Hz.

The resulting finite-dimensional approximation to $H^E(s)$ is

$$\hat{H}^E(s) = \frac{sbY\sqrt{d}}{\alpha_o} \frac{u_3s^3 + u_2s^2 + u_1s + u_0}{r_3s^3 + r_2s^2 + r_1s + r_0} \tag{41}$$

where $u_0, \ldots, u_3$ and $r_0, \ldots, r_3$ are coefficients dependent on K and s_0. The detailed forms of these coefficients are shown in Appendix 1.

Now consider the model reduction for $H^M(s) = N'_3(s)/D'_1(s)$. When there is no tip mass, $N'_3(s)$ and $D'_1(s)$ are denoted by equations (35) and (36), respectively. First, recall that

$$\begin{aligned} N'_3(s) &= 2p(s)[\cos(p(s)L)\sinh(p(s)L) - \cosh(p(s)L)\sin(p(s)L)] \\ &= 2\sqrt[4]{r_s}[\cos(\sqrt[4]{r_s}L)\sinh(\sqrt[4]{r_s}L) - \cosh(\sqrt[4]{r_s}L)\sin(\sqrt[4]{r_s}L)] \end{aligned} \tag{42}$$

where

$$r_s = \frac{(C_a + ms)s^2}{4Is(Y + C_ss)} = \frac{s(C_a + ms)}{4I(Y + C_ss)} \tag{43}$$

Similarly, one can rewrite $D'_1(s)$ as

$$D'_1(s) = \cosh^2(\sqrt[4]{r_s}L) + \cos^2(\sqrt[4]{r_s}L) \tag{44}$$

It is found that good approximation of $H^M(s)$ can be achieved by using Taylor series expansion for $N'_3(s)$ and $D'_1(s)$ separately. Considering up to the second-order Taylor series, which provides satisfactory approximation with minimal complexity, we can get the following approximation to $H^M(s)$ around $r_s = r_0$

$$\hat{H}^M(s) \approx \frac{b_2(r_s - r_0)^2 + b_1(r_s - r_0) + b_0}{d_2(r_s - r_0)^2 + d_1(r_s - r_0) + d_0} \tag{45}$$

for some coefficients b_0, b_1, b_2 and d_0, d_1, d_2. The detailed expressions for these coefficients are given in Appendix 2. Based on the experimental results of

parameter identification (see section "Parameter identification and model validation"), $|r_s|$ is of the order from 10^5 to 10^7, so the value of r_0 can be chosen with large flexibility. Simulation results indicate that any real number of r_0 from 0.01 to 10^6 will give almost the same good approximation results. Without the loss of generality, we take $r_0 = 1000$ in this article.

According to the parameter identification result, $C_a \ll m|s|$, when the frequency is 10 Hz or above, which enables one to make the approximation

$$r_s \approx \frac{ms^2}{4I(Y + C_s s)} \tag{46}$$

Substituting equation (46) into equation (45), we have

$$
\hat{H}^M(s) = \frac{b_2(\frac{ms^2}{4I(Y+C_s s)} - r_0)^2 + b_1(\frac{ms^2}{4I(Y+C_s s)} - r_0) + b_0}{d_2(\frac{ms^2}{4I(Y+C_s s)} - r_0)^2 + d_1(\frac{ms^2}{4I(Y+C_s s)} - r_0) + d_0}
$$
$$
= \frac{b'_4 s^4 + b'_3 s^3 + b'_2 s^2 + b'_1 s + b'_0}{d'_4 s^4 + d'_3 s^3 + d'_2 s^2 + d'_1 s + d'_0} \tag{47}
$$

for some coefficients $b'_0, \ldots, b'_4$ and $d'_0, \ldots, d'_4$. The detailed expressions for these coefficients are given in Appendix 2.

Combining equations (41) and (47) leads to a reduced model for a base-excited IPMC sensors

$$
\hat{H}(s) = \hat{H}^E(s)\hat{H}^M(s) = \frac{sbY\sqrt{d}}{\alpha_o} \frac{u_3 s^3 + u_2 s^2 + u_1 s + u_0}{r_3 s^3 + r_2 s^2 + r_1 s + r_0}
$$
$$
\cdot \frac{b'_4 s^4 + b'_3 s^3 + b'_2 s^2 + b'_1 s + b'_0}{d'_4 s^4 + d'_3 s^3 + d'_2 s^2 + d'_1 s + d'_0} \tag{48}
$$

Note that this reduced model of equation (48) is still a physics-based model and geometrically scalable since it is expressed in terms of fundamental physical parameters and sample dimensions. Such a characteristic distinguishes this model from other low-order, black-box or gray-box models. Figure 5 shows the comparison of simulation results between the original, infinite-dimensional model $H(s)$ and the reduced model $\hat{H}(s)$, for the IPMC sensor with zero tip mass. From Figure 5, it can been seen that although there are some noticeable discrepancies at the high end of the frequency range, overall the reduction from equation (33) to equation (48) does not produce significant approximation error, indicating the feasibility of the proposed model reduction strategy.

In order to further validate the proposed model and the reduction approach, we have excited the IPMC base with a multitone oscillatory signal, which has not been used in the parameter identification process. In particular, the used excitation signal is $u(t) = 0.1742 \sin(2\pi \cdot 60t + 0.5) + 0.1944 \sin(2\pi \cdot 80t) + 0.0621 \sin(2\pi \cdot 100t + 1)$ mm. The measured base excitation is fed to the reduced model, to predict the sensing signal in the time domain. Figure 6 shows the
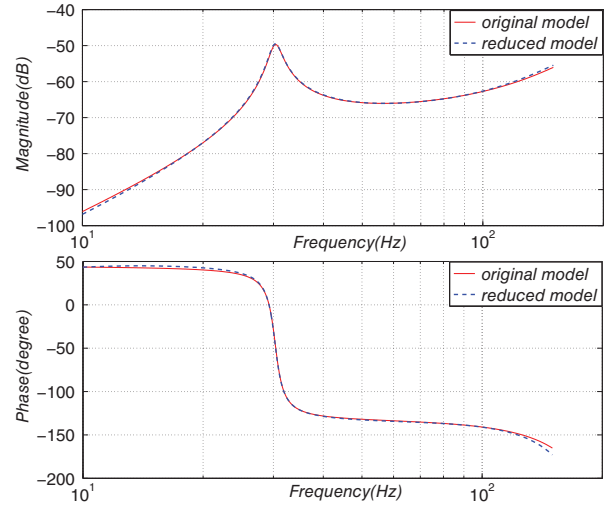

Figure 5. Comparison of simulation results between the original model $H(s)$ and the reduced model $\hat{H}(s)$ for the base-excited IPMC sensor.
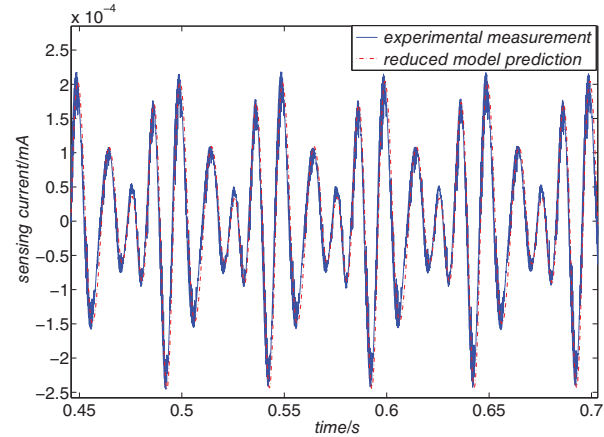IPMC: ionic polymer–metal composite.

Figure 6. Prediction of the sensing response versus experimental measurement under a multitone oscillatory excitation, when no tip mass is added.

comparison between the measured and predicted sensing currents, where one can see that excellent agreement in both magnitude and phase is achieved. The reduced model will be used for reconstructing the base excitation stimulus through inverse compensation.

Inverse compensation scheme

The inversion algorithm

An important motivation for deriving a transfer function-type sensing model $H(s)$ for base-excited IPMC sensors is its potential use in structural vibration monitoring. In such applications, we need to infer the underlying mechanical stimulus given the current output of an IPMC sensor. In particular, we are interested

in reconstructing the original mechanical signal $u(t)$ based on the sensor output $i(t)$, either online or off-line. Intuitively, the reconstruction can be achieved by inverting the sensing model

$$U(s) = H_{inv}(s)I(s)$$

where $H_{inv}(s)$ represents the inverse dynamics

$$H_{inv}(s) = \frac{1}{\hat{H}(s)}$$

However, the reduced model $\hat{H}(s)$ obtained is of nonminimum phase (having zeros with positive real parts), and thus, the resulting $H_{inv}(s)$ would be unstable and not implementable. For example, based on the parameters in section "Parameter identification and model validation," the resulting transfer function $\hat{H}(s)$ has three stable zeros (-35.98, -500.2, -6965) and one zero at the origin for the mechanoelectric portion of $\hat{H}^E(s)$, and two stable zeros (-1176, -9.38) and two unstable zeros ($+2096$, $+9.413$) for the beam dynamics portion of $\hat{H}^M(s)$. Note that those zeros that are on the origin or close to the origin are also problematic for inverse implementation.

In this article, we explore the use of techniques for stable inversion of nonminimum-phase systems (Devasia et al., 1996; Ganley et al., 2011) to reconstruct the base excitation on the IPMC sensor using the sensing current output. It is first assumed that $\hat{H}(s)$ is hyperbolic, meaning that it has no zeros on the imaginary axis. Therefore, the zeros at the origin and close to the origin will be treated separately. The inversion problem is formulated as follows: given the sensor output function $i(t)$, $0 \leqslant t < \infty$, find the function $u(t)$, $0 \leqslant t < \infty$, such that

$$i(t) = \hat{H}(s)[u](t) \quad (49)$$

where the mixed frequency–time domain notation $\hat{H}(s)[u](t)$ represents the signal obtained by passing $u(\cdot)$ through the system $\hat{H}(s)$. If $\hat{H}(s)$ is a minimum-phase system, the solution $u(t)$ can be computed easily using

$$u(t) = H_{inv}(s)[i](t) \quad (50)$$

For a nonminimum phase $\hat{H}(s)$, as in the case of an IPMC sensor, $H_{inv}(s)$ contains unstable poles, and thus, the algorithm above is not implementable. To solve the inversion problem, we decompose $H_{inv}(s) = H_s(s) + H_u(s)$, where all poles of $H_s(s)$ have negative real parts, while all poles of $H_u(s)$ have positive real parts. Note that by the hyperbolic assumption on $\hat{H}(s)$, $H_{inv}(s)$ has no poles on the imaginary axis. The solution $u(t)$ to the inversion problem will correspondingly have two parts: $u(t) = u_s(t) + u_u(t)$, where $u_s(t) = H_s(s)[i](t)$ and $u_u(t)$ is computed as follows (see Figure 7 for illustration).
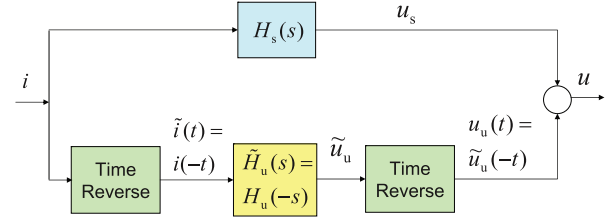

Figure 7. Schematic of the stable inversion algorithm for a nonminimum-phase system.

We first mirror the signal $i(t)$ with respect to $t = 0$ and obtain $\tilde{i}(t) = i(-t)$. Then, we pass the time-reversed signal $\tilde{i}$ through a stable system $\tilde{H}_u(s) \triangleq H_u(-s)$ and get $\tilde{u}_u = \tilde{H}_u(s)[\tilde{i}](t)$. We then obtain u_u from $\tilde{u}_u$ by reversing the time again, $u_u(t) = \tilde{u}_u(-t)$. Note that evaluating $u_u(t^*)$ for some t^*, requires knowing $i(t)$, for all $t > t^*$. Therefore, the essence of stable inversion of a nonminimum-phase system lies in converting an originally unstable but causal system to a stable but noncausal system. The stable inversion algorithm can be easily adapted so that it requires a finite amount of "preview time" (as opposed to all time into the future) (Devasia et al., 1996; Ganley et al., 2011) with arbitrarily small approximation errors.

Finally, we need to deal with the zero of $\hat{H}(s)$ at the origin, we approximate it by $-\varepsilon > 0$. In our implementation, ε is chosen to be -0.1. This is reasonable since $s + 0.1 \approx s$ within the considered frequency range of 10–150 Hz.

Simulation results

The inversion scheme for the reduced model is first illustrated through reconstructing the mechanical excitation from sensing current in simulation. A multitone oscillatory base excitation signal is generated, where $u(t) = 0.2 \sin(35 \cdot 2\pi t + \pi/3) + 0.1 \sin(20 \cdot 2\pi t + \pi/4) + 0.05 \sin(15 \cdot 2\pi t)$ mm. The resulting sensing current, evaluated using the reduced model, is then used to infer the base displacement using the proposed inverse compensation scheme. Figure 8 shows that good agreement has been achieved between the predicted and original base excitation signals, indicating that the inverse compensation scheme is effective. The slight mismatch is likely due to the approximation of s by $s + 0.1$, and investigation is underway to understand how to minimize the mismatch.

Structural vibration monitoring

The proposed model and inverse compensation scheme are further validated in structural vibration monitoring experiments. In these experiments, we use the current output of an IPMC sensor to reconstruct the time domain vibration signal on a mechanical structure. Figure 9 shows the experimental setup. The base of the IPMC beam is attached to an aluminum frame structure. Two types of stimuli are applied to the structure.
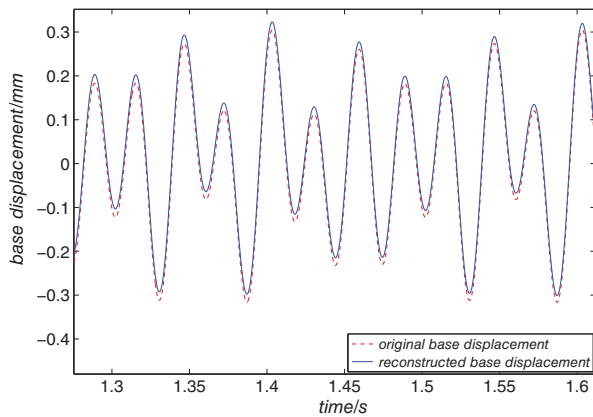
Figure 8. Simulation results on the comparison of the base excitation signal reconstructed through model-based inverse compensation with the actual signal.
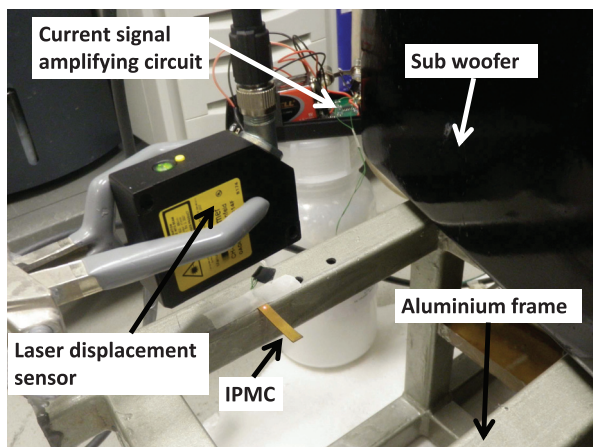

Figure 9. Experimental setup for structural vibration monitoring. IPMC: ionic polymer–metal composite.

First, a periodic stimulus is generated by a subwoofer that sits on the aluminum structure. The subwoofer receives oscillatory actuation signals generated from the dSPACE system and produces the corresponding mechanical vibration, which is then transferred to the aluminum frame. The second type of stimulus is an impact, generated by hitting the frame with an iron hammer. A laser displacement sensor is amounted above the base of the IPMC sensor, detecting the actual mechanical displacement at the base. The same current-amplifier circuit in Figure 2 is used to measure the IPMC sensing current. The reconstructed mechanical stimulus signal will be compared with the measured vibration displacement.

Experiment results. Figure 10 shows the experimental result for the case of a multitone oscillatory excitation generated by the subwoofer. As we can see from Figure 10, there is a reasonable agreement at the steady state between the reconstructed vibration signals and the measured displacement from laser sensor. Figure 11
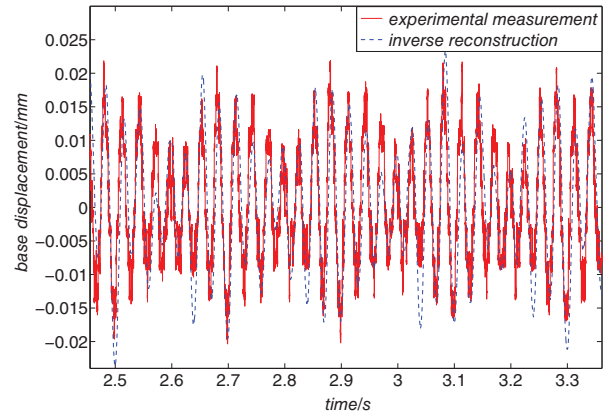

Figure 10. Experimental results on structural vibration monitoring: comparison of the reconstructed signal at the base with the actual multitone oscillatory excitation.
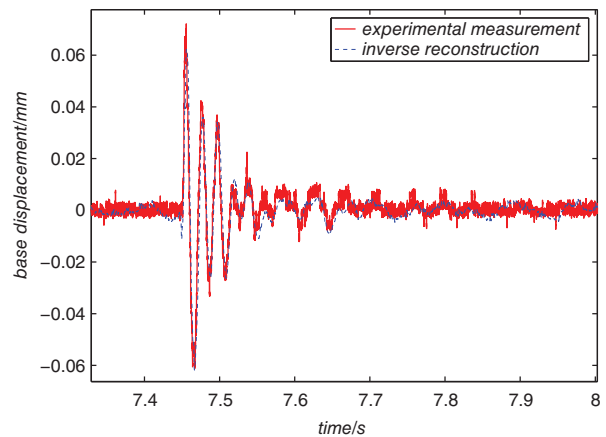

Figure 11. Experimental results on structural vibration monitoring: comparison of the reconstructed signal at the base with the actual impact excitation.

shows the comparison between the measured base vibration with its sensor-based reconstruction for the case of an impact stimulus, where good agreement is achieved again. Notice that the temperature and the humidity level of the ambient environment in which these experiments are conducted might be different from those for the parameter identification process, which can contribute to the errors between the reconstructed signals and the real measurement. As we discussed in section "Parameter identification and model validation," impacts of these factors can be mitigated in several ways.

Conclusion

In this article, we have developed a dynamic model for a base-excited IPMC sensor in air, which comprises a cascade of a mechanical module accounting for the vibration dynamics and an electrical module accounting for the charge dynamics within the IPMC. The model has a closed form and is geometrically scalable. Schemes have

been developed to approximate the original infinite-dimensional model with one that is finite-dimensional, to facilitate practical use in sensing and feedback control applications. Experimental results have validated the mechanical vibration model and the overall sensing model. In addition, an inverse compensation scheme has been described and illustrated with simulation results and structural monitoring experiments.

Future work can be pursued in several directions. First, in this article, we have assumed perfectly conducting electrodes. A natural extension would be to incorporate the effect of surface resistance so that the model is able to predict accurately the response of IPMC sensors with nonideal electrodes. Second, as we show in this article, the air-damping and added-mass effects are negligible when the IPMC sensor is operated in air. This may not be the case if the sensor is operated in an aqueous environment, where nonlinear damping and added-mass effects are nonnegligible as shown in the works of Aureli and Porfiri (2010) and Aureli et al. (2012). In that case, our model can be potentially extended to incorporate those effects following the approach by Aureli et al. (2012) and Aureli and Porfiri (2010). Finally, we will continue to investigate effective packaging schemes for IPMC sensors to minimize the influence of environmental humidity on their behaviors, which will bring IPMC sensors closer to practical applications such as monitoring of bridges and other structures.

Funding

References

Abdulsadda AT and Tan X (2011) Underwater source localization using an IPMC-based artificial lateral line. In: *IEEE international conference on robotics and automation*, 9–13 May 2011, Shanghai, China, pp. 2719–2724. Piscataway, NJ: IEEE.

Abdulsadda AT and Tan X (2012) An artificial lateral line system using IPMC sensor arrays. *International Journal of Smart and Nano Materials* 3: 226–242.

Abdulsadda AT, Zhang F and Tan X (2011) Localization of source with unknown amplitude using IPMC sensor arrays. In: *Proceedings of SPIE: electroactive polymer actuators and devices (EAPAD) XIII* (eds Y Bar-Cohen and F Carpi), San Diego, CA, 6–10 March 2011, p. 797627 (11 pp.). Bellingham, WA: SPIE.

Aureli M and Porfiri M (2010) Low frequency and large amplitude oscillations of cantilevers in viscous fluids. *Applied Physics Letters* 96(16): 164102.

Aureli M and Porfiri M (2013) Nonlinear sensing of ionic polymer metal composites. *Continuum Mechanics and Thermodynamics*. 25(2-4): 273–310.

Aureli M, Basaran ME and Porfiri M (2012) Nonlinear finite amplitude vibrations of sharp-edged beams in viscous fluids. *Journal of Sound and Vibration* 331(7): 1624–1654.

Aureli M, Kopman V and Porfiri M (2010a) Free-locomotion of underwater vehicles actuated by ionic polymer metal composites. *IEEE/ASME Transactions on Mechatronics* 15(4): 603–614.

Aureli M, Prince C, Porfiri M, et al. (2010b) Energy harvesting from base excitation of ionic polymer metal composites in fluid environments. *Smart Materials and Structures* 19(1): 015003.

Bahramzadeh Y and Shahinpoor M (2011) Dynamic curvature sensing employing ionic-polymer-metal composite sensors. *Smart Materials and Structures* 20: 094011.

Baker GA and Graves-Morris P (1996) *Padé Approximants*. New York: Cambridge University Press.

Bar-Cohen Y (2001) *Electroactive Polymer Actuators as Artificial Muscles: Reality, Potential and Challenges*. Bellingham, WA: SPIE.

Bonomo C, Fortuna L, Giannone P, et al. (2006) A model for ionic polymer metal composites as sensors. *Smart Materials and Structures* 15: 749–758.

Bonomo C, Fortuna L, Giannone P, et al. (2008) A resonant force sensor based on ionic polymer metal composites. *Smart Materials and Structures* 17(1): 015014.

Brufau-Penella J, Puig-Vidal M, Giannone P, et al. (2008) Characterization of the harvesting capabilities of an ionic polymer metal composite device. *Smart Materials and Structures* 17(1): 015009.

Brunetto P, Fortuna L, Giannone P, et al. (2011) Characterization of the temperature and humidity influence on ionic polymer-metal composites as sensors. *IEEE Transactions on Instrumentation and Measurement* 60(8): 2951–2958.

Buechler MA and Leo DJ (2007) Characterization and variational modeling of ionic polymer transducers. *Journal of Vibration and Acoustics: Transactions of the ASME* 129: 113–120.

Bufalo GD, Placidi L and Porfiri M (2008) A mixture theory framework for modeling the mechanical actuation of ionic polymer metal composites. *Smart Materials and Structures* 17(4): 045010.

Chen Z and Tan X (2010) Monolithic fabrication of ionic polymer-metal composite actuators capable of complex deformation. *Sensors and Actuators A: Physical* 157(2): 246–257.

Chen Z, Shatara S and Tan X (2010) Modeling of biomimetic robotic fish propelled by an ionic polymer-metal composite caudal fin. *IEEE/ASME Transactions on Mechatronics* 15(3): 448–459.

Chen Z, Shen Y, Xi N, et al. (2007a) Integrated sensing for ionic polymer-metal composite actuators using PVDF thin films. *Smart Materials and Structures* 16(2): S262–S271.

Chen Z, Tan X, Will A, et al. (2007b) A dynamic model for ionic polymer-metal composite sensors. *Smart Materials and Structures* 16: 1477–1488.

Clough RW and Penzien J (1975) *Dynamics of Structures*. New York: McGraw-Hill.

De Gennes PG, Okumura K, Shahimpoor M, et al. (2000) Mechanoelectric effects in ionic gels. *Europhysics Letters* 50(4): 513–518.

Devasia S, Chen D and Paden B (1996) Nonlinear inversion-based output tracking. *IEEE Transactions on Automatic Control* 41(7): 930–942.

Erturk A and Inman DJ (2011) *Piezoelectric Energy Harvesting*. 1st ed. Chichester, UK: John Wiley & Sons, Ltd.

Farinholt K and Leo DJ (2004) Modeling of electromechanical charge sensing in ionic polymer transducers. *Mechanics of Materials* 36: 421–433.

Farinholt KM, Pedrazas NA, Schluneker DM, et al. (2009) An energy harvesting comparison of piezoelectric and ionically conductive polymers. *Journal of Intelligent Material Systems and Structures* 20(5): 633–642.

Ganley T, Hung DLS, Zhu G, et al. (2011) Modeling and inverse compensation of temperature-dependent ionic polymer-metal composite sensor dynamics. *IEEE/ASME Transactions on Mechatronics* 16(1): 80–89.

Ghosh AK (1986) Vibration of a cantilever beam on a composite support with base excitation. *Journal of Sound and Vibration* 105(1): 91–99.

Kim KJ and Shahinpoor M (2003) Ionic polymer-metal composites: II. Manufacturing techniques. *Smart Materials and Structures* 15: 65–79.

Lei H, Li W and Tan X (2012a) Microfabrication of IPMC cilia for bio-inspired flow sensing. In: Bar-Cohen Y (ed.) *Electroactive Polymer Actuators and Devices (EAPAD) XIV*, vol. 8340. San Diego, CA, 11–15 March 2012, p. 83401A (9 pp.). Bellingham, WA: SPIE.

Lei H, Li W, Zhu G, et al. (2012b) Evaluation of encapsulated IPMC sensor based on thick parylene coating. In: *Proceedings of ASME 2012 conference on smart materials, adaptive structures and intelligent systems*, 19–21 September, 2012 Stone Mountain, GA, SMASIS2012-7975. New York, NY: ASME.

Lim C, Lei H and Tan X (2012) A dynamic, physics-based model for base-excited IPMC sensors. In: Bar-Cohen Y (ed.) *Electroactive Polymer Actuators and Devices (EAPAD) XIV*, vol. 8340. San Diego, CA, 11–15 March 2012, p. 83400H (12 pp.). Bellingham, WA: SPIE.

Nemat-Nasser S and Li J (2000) Electromechanical response of ionic polymer-metal composites. *Journal of Applied Physics* 87(7): 3321–3331.

Newbury K (2002) *Characterization, modeling, and control of ionic polymer transducers*. PhD Dissertation, Virginia Polytechnic Institute and State University, Blacksburg, VA.

Newbury KM and Leo DJ (2002) Electromechanical modeling and characterization of ionic polymer benders. *Journal of Intelligent Material Systems and Structures* 13: 51–60.

Paola B, Fortuna L, Giannone P, et al. (2008) IPMCs as vibration sensors. In: *Proceedings of the IEEE international instrumentation and measurement technology conference*, 12–15 May 2008, pp. 2065–2069, British Columbia, Canada.

Peterson SD and Porfiri M (2012) Energy exchange between a vortex ring and an ionic polymer metal composite. *Applied Physics Letters* 100: 114102.

Porfiri M (2009) An electromechanical model for sensing and actuation of ionic polymer metal composites. *Smart Materials and Structures* 18(1): 015016.

Sader JE (1998) Frequency response of cantilever beams immersed in viscous fluids with applications to the atomic force microscope. *Journal of Applied Physics* 84(1): 64–76.

Shahinpoor M and Kim KJ (2001) Ionic polymer-metal composites: I. Fundamentals. *Smart Materials and Structures* 10: 819–833.

Shahinpoor M and Kim KJ (2004) Ionic polymer-metal composites: III. Modeling and simulation as biomimetic sensors, actuators, transducers, and artificial muscles. *Smart Materials and Structures* 13: 1362–1388.

Tadokoro S, Yamagami S and Ozawa M (1999) Soft micromanipulation device with multiple degrees of freedom consisting of high polymer gel actuators. In: *Proceedings of the IEEE*

international conference on micro electro mechanical systems, Orlando, Florida, USA, 17–21 January 1999, pp. 42.

Takagi K, Kamamichi N, Stoimenov B, et al. (2008) Frequency response characteristics of IPMC sensors with current/voltage measurements. In: *Proceedings of SPIE*, vol. 6927, Bellingham, WA, 9–14 March 2008, San Diego, CA, p. 692724. Bellingham, WA: SPIE.

Wallmersperger T, Leo D and Kothera C (2007) Transport modeling in ionomeric polymer transducers and its relationship to electromechanical coupling. *Journal of Applied Physics* 101(2): 4912–4921.

Zangrilli U and Weiland LM (2011) Prediction of the ionic polymer transducer sensing of shear loading. *Smart Materials and Structures* 20(9): 094013.

Appendix I

Derivation of equation (41)

Based on the algorithm of the Padé approximation (Baker and Graves-Morris, 1996), for $f(s) = \sqrt{s + K}$ expanded around $s = s_0$, one gets equation (40) as

$$f(s) = \sqrt{s + K} \approx \frac{\sum_{l=0}^{m} q_l(s - s_0)^l}{1 + \sum_{k=1}^{n} d_k(s - s_0)^k} \quad (51)$$

For $m = 3$, $n = 2$

$$d_1 = \frac{a_2 a_5 - a_3 a_4}{a_3^2 - a_2 a_4}$$

$$d_2 = \frac{a_4^2 - a_3 a_5}{a_3^2 - a_2 a_4}$$

$$q_0 = a_0$$

$$q_1 = a_1 + a_0 d_1$$

$$q_2 = a_2 + a_1 d_1 + a_0 d_2$$

$$q_3 = a_3 + a_2 d_1 + a_1 d_2$$

where $a_0, \ldots, a_5$ are calculated as

$$a_0 = f(s_0) = \sqrt{s_0 + K}$$

$$a_1 = f^{(1)}(s_0) = \frac{1}{2\sqrt{s_0 + K}}$$

$$a_2 = f^{(2)}(s_0) = \frac{-1}{8\sqrt{(s_0 + K)^3}}$$

$$a_3 = f^{(3)}(s_0) = \frac{3}{48\sqrt{(s_0 + K)^5}}$$

$$a_4 = f^{(4)}(s_0) = \frac{-15}{384\sqrt{(s_0 + K)^7}}$$

$$a_5 = f^{(5)}(s_0) = \frac{105}{3840\sqrt{(s_0 + K)^9}}$$

and $f^{(k)}$ denotes the kth derivative of f. Substituting equation (51) into equation (39), we have

$$\hat{H}^E(s) = \frac{sbY\sqrt{d}}{\alpha_o} \frac{\frac{\sum_{l=0}^{3} q_l(s-s_0)^l}{1 + \sum_{k=1}^{2} d_k(s-s_0)^k} h - \sqrt{d}}{s + K}$$

$$= \frac{sbY\sqrt{d}}{\alpha_o} \frac{u_3 s^3 + u_2 s^2 + u_1 s + u_0}{r_3 s^3 + r_2 s^2 + r_1 s + r_0}$$

which is equation (41) with

$$u_3 = hq_3$$
$$u_2 = hq_2 - 3hq_3 s_0 - \sqrt{d} d_2$$
$$u_1 = 3hq_3 s_0^2 - 2hq_2 s_0 + 2\sqrt{d} d_2 s_0 - \sqrt{d} d_1$$
$$u_0 = -hq_3 s_0^3 + (hq_2 - \sqrt{d} d_2) s_0^2$$
$$+ (\sqrt{d} d_1 s_0 - hq_1) s_0 + hq_0 - \sqrt{d}$$
$$r_3 = d_2$$
$$r_2 = d_1 - 2d_2 s_0 + Kd_2$$
$$r_1 = d_2 s_0^2 - (d_1 + 2Kd_2) s_0 + 1 + Kd_1$$
$$r_0 = Kd_2 s_0^2 - Kd_1 s_0 + K$$

Appendix 2

Derivation of equation (47)

From equation (42), one can perform Taylor expansion about $r_s = r_0$ to approximate $N'_3(s)$, considering up to the second-order terms

$$N'_3(s) \approx N'_3(r_s = r_0) + \frac{dN'_3(s)}{dr_s}\Big|_{r_s = r_0}(r_s - r_0)$$
$$+ \frac{d^2 N'_3(s)}{dr_s^2}\Big|_{r_s = r_0} \frac{(r_s - r_0)^2}{2!}$$
$$= b_0 + b_1(r_s - r_0) + b_2(r_s - r_0)^2 \quad (52)$$

where

$$R_0 = \sqrt[4]{r_0} L$$
$$b_0 = N'_3(r_s = r_0)$$
$$= 2\sqrt[4]{r_0}[\cos(R_0)\sinh(R_0) - \cosh(R_0)\sin(R_0)]$$
$$b_1 = \frac{dN'_3(s)}{dr_s}\Big|_{r_s = r_0}$$
$$= \frac{\cos(R_0)\sinh(R_0) - \cosh(R_0)\sin(R_0)}{2\sqrt[4]{r_0^3}}$$
$$- \frac{L\sin(R_0)\sinh(R_0)}{\sqrt{r_0}}$$
$$b_2 = \frac{1}{2!}\frac{d^2 N'_3(s)}{dr_s^2}\Big|_{r_s = r_0}$$
$$= \frac{L\sin(R_0)\sinh(R_0)}{8\sqrt{r_0^3}}$$
$$- \frac{3[\cos(R_0)\sinh(R_0) - \cosh(R_0)\sin(R_0)]}{16\sqrt[4]{r_0^7}}$$
$$- \frac{L^2[\cos(R_0)\sinh(R_0) + \cosh(R_0)\sin(R_0)]}{8\sqrt[4]{r_0^5}}$$

Similarly, from equation (44), one can approximate $D'_1(s)$ by using the Taylor series expansion

$$D'_1(s) \approx d_0 + d_1(r_s - r_0) + d_2(r_s - r_0)^2$$

where

$$d_0 = D'_1(r_s = r_0) = \cosh^2(R_0) + \cos^2(R_0)$$
$$d_1 = \frac{dD'_1(s)}{dr_s}\Big|_{r_s = r_0} = \frac{-L[\sin(2R_0) - \sinh(2R_0)]}{4\sqrt[4]{r_0^3}}$$
$$d_2 = \frac{1}{2!}\frac{d^2 D'_1(s)}{dr_s^2}\Big|_{r_s = r_0}$$
$$= \frac{L[3\sin(2R_0) - 3\sinh(2R_0) - 2R_0\cos(2R_0) + 2R_0\cos(2R_0)]}{32\sqrt[4]{r_0^7}}$$

Substituting equation (46) into equation (45), we have equation (47) as

$$\hat{H}^M(s) = \frac{b_2(\frac{ms^2}{4I(Y+C_s s)} - r_0)^2 + b_1(\frac{ms^2}{4I(Y+C_s s)} - r_0) + b_0}{d_2(\frac{ms^2}{4I(Y+C_s s)} - r_0)^2 + d_1(\frac{ms^2}{4I(Y+C_s s)} - r_0) + d_0}$$

$$= \frac{b'_4 s^4 + b'_3 s^3 + b'_2 s^2 + b'_1 s + b'_0}{d'_4 s^4 + d'_3 s^3 + d'_2 s^2 + d'_1 s + d'_0}$$

where

$$b'_4 = b_2 m^2$$
$$b'_3 = 4b_1 mIC_s - 8b_2 mr_0 IC_s$$
$$b'_2 = 4b_1 mIY - 8b_2 mr_0 IY + 16I^2 C_s^2(b_2 r_0^2 + b_0 - b_1 r_0)$$
$$b'_1 = 32I^2 YC_s(b_2 r_0^2 + b_0 - b_1 r_0)$$
$$b'_0 = 16I^2 Y^2(b_2 r_0^2 + b_0 - b_1 r_0)$$
$$d'_4 = d_2 m^2$$
$$d'_3 = 4d_1 mIC_s - 8d_2 mr_0 IC_s$$
$$d'_2 = 4d_1 mIY - 8d_2 mr_0 IY + 16I^2 C_s^2(d_2 r_0^2 + d_0 - d_1 r_0)$$
$$d'_1 = 32I^2 YC_s(d_2 r_0^2 + d_0 - d_1 r_0)$$
$$d'_0 = 16I^2 Y^2(d_2 r_0^2 + d_0 - d_1 r_0)$$